

## Clustering and interfacial segregation of radiogenic Pb in a mineral host-inclusion system: Tracing two-stage Pb and trace element mobility in monazite inclusions in rutile

RICK VERBERNE<sup>1,2,3,\*</sup>, STEVEN M. REDDY<sup>2,3,†</sup>, DENIS FOUGEROUSE<sup>2,3,‡</sup>,  
ANNE-MAGALI SEYDOUX-GUILLAUME<sup>5</sup>, DAVID W. SAXEY<sup>2,3</sup>, WILLIAM D.A. RICKARD<sup>2</sup>,  
ZAKARIA QUADIR<sup>4</sup>, AND CHRIS CLARK<sup>3</sup>

<sup>1</sup>Centre for Star and Planet Formation, Globe Institute, University of Copenhagen, Øster Voldgade 5–7, DK-1350 Copenhagen, Denmark

<sup>2</sup>Geoscience Atom Probe, John de Laeter Centre, Curtin University, Perth, Western Australia 6845, Australia

<sup>3</sup>School of Earth and Planetary Sciences, Curtin University, Perth, Western Australia 6845, Australia

<sup>4</sup>Microscopy and Microanalysis Facility, John de Laeter Centre, Curtin University, GPO Box U1987, Perth, Western Australia 6845, Australia

<sup>5</sup>UJM-Saint-Etienne, LGL-TPE UMR5276 CNRS, 42023 Saint-Étienne, France

### ABSTRACT

Accessory minerals like zircon, rutile and monazite are routinely studied to inform about the timing and nature of geological processes. These studies are underpinned by our understanding of the transfer processes of trace elements and the assumption that the isotopic systems remain undisturbed. However, the presence of microstructures or Pb-bearing phases in minerals can lead to the alteration of the Pb isotopic composition. To gain insight into the relationship between Pb isotopic alterations from inclusions and microstructures, this study focused on inclusions from an ultra-high-temperature metamorphic rutile. The studied inclusions are submicrometer monazites, a common mineral rich in Pb but normally not present in rutile. The sample is sourced from Mt. Hardy, Napier Complex, East Antarctica, an ultra-high-temperature (UHT) metamorphic terrane. By applying correlative analytical techniques, including electron backscatter diffraction mapping, transmission electron microscopy (TEM), and atom probe tomography, it is shown that monazite inclusions are often in contact with low-angle boundaries and yield no preferred orientation. TEM analysis shows the monazite core has a mottled texture due to the presence of radiation damage and nanoclusters associated with the radiation damage defects that are rich in U, Pb, and Ca. Some monazites exhibit a core-rim structure. The rim yields clusters composed of Ca- and Li-phosphate that enclose Pb nanoclusters that are only present in small amounts compared to the core, with Pb likely diffused into the rutile-monazite interface. These textures are the result of two stages of Pb mobility. Initial Pb segregation was driven by volume diffusion during UHT metamorphism (2500 Ma). The second stage is a stress-induced recrystallization during exhumation, leading to recrystallization of the monazite rim and trace element transport. The isotopic signature of Pb trapped within the rutile-monazite interface constrains the timing of Pb mobility to ca. 550 Ma.

**Keywords:** Rutile, monazite, Pb mobility, atom probe tomography

### INTRODUCTION

Rutile (TiO<sub>2</sub>) is a common accessory mineral that is stable at mid- to lower-crustal metamorphic conditions (Clark et al. 2019; Dachille et al. 1968; Harley 2016). Zr-in-rutile geothermometry and rutile U-Pb geochronology are increasingly used to provide temperature and time constraints on the evolution of metamorphic terranes (Clark et al. 2018; Kooijman et al. 2010; Meinhold 2010; Smye and Stockli 2014; Watson et al. 2006; Zack et al. 2004a). Mineral inclusions in rutile are geologically significant, with inclusions of corundum in rutile providing constraints on growth mechanisms (Daneu et al. 2014), while the molar fraction of Zr-bearing mineral inclusions can be used to re-integrate Zr concentrations for the estimation of peak

metamorphic temperatures (Mitchell and Harley 2017; Pape et al. 2016). The ability of rutile to trap and isolate inclusions from retrograde metamorphic overprints and fluid alteration events may allow inclusion assemblages in rutile to be used to characterize metamorphic conditions in ultrahigh-pressure (UHP) and ultrahigh-temperature (UHT) metamorphic terranes (Hart et al. 2016, 2018).

Despite the uses of inclusion analyses, the presence of small (<1 µm diameter) inclusions in rutile has the potential to compromise compositional and isotopic analysis of the host mineral by common techniques, such as laser ablation inductively coupled plasma mass spectrometry (LA-ICP-MS), which analyzes significantly larger volumes than the inclusion volume. Little is currently known about the geochemistry of sub-micrometer mineral inclusions or how their presence and composition may affect the analysis of the host. In part, this reflects the difficulty in measuring the trace element and isotopic compositions of such small inclusions. Furthermore, there is little information regard-

\* Corresponding author E-mail: rick.verberne89@gmail.com. Orcid <https://orcid.org/0000-0002-5529-1250>

† Orcid <https://orcid.org/0000-0002-4726-5714>

‡ Orcid <https://orcid.org/0000-0003-3346-1121>

ing how such inclusions may evolve as the pressure-temperature conditions of the host rock change over time or if such inclusions are truly isolated from the matrix of the rock in which the host mineral resides. In this contribution, the structural setting and compositional character of micrometer-scale (200–1100 nm) monazite inclusions within ultrahigh-temperature metamorphic rutile are studied to provide some constraints on host-inclusion relationships and determine the mechanisms by which compositional heterogeneity in the inclusion may be developed.

The mobility of Pb in monazite has received significant attention in nanoscale studies using transmitted electron microscopy (TEM) and atom probe tomography (APT) (Bingen and Van Breemen 1998; Fougereuse et al. 2018, 2021a; Grand'Homme et al. 2016; Seydoux-Guillaume et al. 2003, 2012, 2019; Turuani et al. 2022, 2023). However, such studies have typically analyzed the internal parts of large monazite crystals, ignoring the potential complications associated with Pb mobility adjacent to mineral-mineral interfaces that characterize small inclusions.

The complementary use of APT, TEM, and electron back-scattered diffraction (EBSD) provides unique insight into Pb migration within the inclusions (Reddy et al. 2020). The results obtained show evidence for multiple mechanisms of Pb and trace

element mobility, provide important insights into the segregation of Pb to mineralogical grain boundaries, and yield important new observations that influence the interpretation of isotopic data from sub-micrometer monazite grains in a mineral-host system.

## GEOLOGICAL SETTING AND SAMPLE DESCRIPTION

The sample used for this study was collected from Mt. Hardy in the Napier Complex of East Antarctica (Fig. 1a) and is from an Archean Mg-Al rich metapelitic layer. The Napier Complex consists of a suite of Archean (2990–2800 Ma, Black et al. 1986; Harley and Black 1987). ortho- and paragneisses that underwent a complex deformational and metamorphic history including two ultrahigh-temperature (UHT) metamorphic events at ca. 2850 and ca. 2580 Ma with their timing constraint by zircon dating. (Clark et al. 2018; Harley 2016; James and Black 1981; Sheraton et al. 1987). The ca. 2500 Ma UHT event is widely believed to have resulted in the formation of the highest regional-scale temperatures for exposed crustal rocks on Earth, with temperature estimates coming from the region where Mt. Hardy is located of between 1050–1120 °C (Harley and Motoyoshi 2000; Hokada 2001). These high temperatures are thought to have persisted for in excess of 100 Myr (Clark et al. 2018; Harley 2016). Two

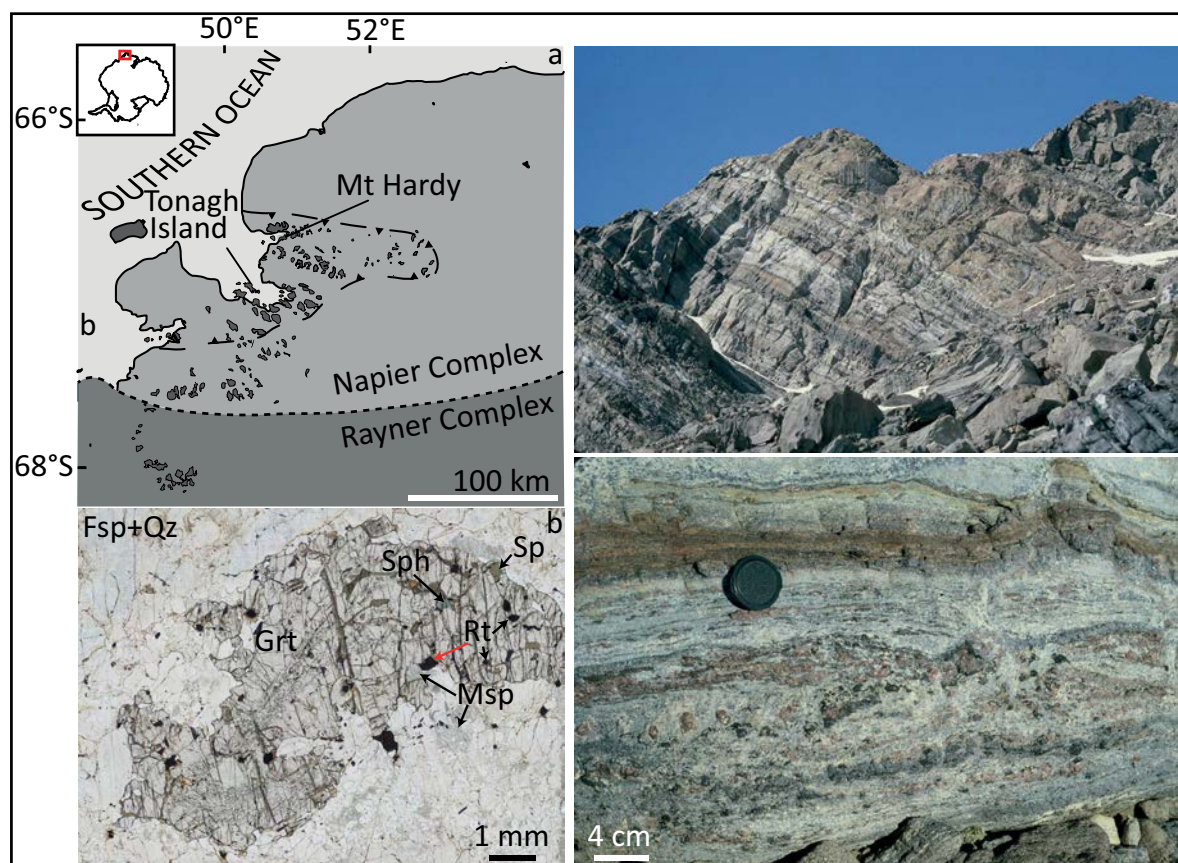


**FIGURE 1.** (a) Simplified geological map of the Napier complex after Carson et al. (2002). (b) Photomicrograph showing the location of the analyzed rutile grain within the thin section. The rutile is in contact with a coarse garnet that hosts rutile, spinel, and sapphirine inclusions and resides in a matrix of mesoperthite, quartz, and minor biotite. (c and d) Field images of the outcrop at Mt. Hardy. The photos show the large-scale foliation present at the sample locality with close-up photo of a leucosome rich in coarse-grained garnet and quartz from which the sample was prepared. Sample coordinates 66°49'04.2"S 50°42'60.0"E. Fsp = feldspar; Grt = garnet; Sph = sapphirine; Sp = spinel; Rt = rutile; Msp = mesoperthite. Red arrow indicates studied rutile. (Color online.)

younger events, mostly in the southern region of the Napier Complex have been described by Black et al. (1983, 1984). Zircon and monazite U-Pb dating constrain an amphibolite-facies metamorphic event to take place between 1073–1094 Ma. Rb-Sr ages record new magmatic and hydrothermal activity to take place around 522 Ma (Black et al. 1983). A study on galena inclusions in monazite (Turuani et al. 2022) shows the latter event (522 Ma) was more localized, while the event at 1073 Ma was more pervasive within the Napier Complex.

The sample comprises dry residual layers of porphyroblastic garnet-cordierite-spinel-sapphirine-osumilite (now replaced by symplectites of K-feldspar-cordierite-dendritic orthopyroxene) and quartz-mesoperthite leucosomes (Fig. 1b). Rutile occurs as inclusions in garnet and within both the residual layers and leucosomes; rutile is inferred to form part of the peak UHT assemblage. In this sample, a population of sector-zoned “soccer-ball” type zircons interpreted to be metamorphic in origin yielded a concordia age of  $2492 \pm 7$  Ma and a Ti-in-zircon temperature of  $915 \pm 30$  °C (Clark et al. 2018). The monazite inclusions reside in two rutile grains. The monazites studied were extracted from rutile in direct contact with garnet, mesoperthite, and traces of biotite. Submicrometer monazite inclusions are also present in the biotite present in the direct vicinity of the rutile grain of interest. No large monazite grains are present within this sample. However, the earliest monazite in the Napier complex likely crystallized around 3070 Ma (Black et al. 1984).

## METHODS

### Electron backscatter diffraction and energy-dispersive X-ray spectroscopy

The thin section has previously been analyzed by LA-ICP-MS. Following LA-ICP-MS, the thin section was re-polished carbon-coated, and analyzed by scanning electron microscope (SEM). SEM characterization was undertaken on a TESCAN Mira3 field emission scanning electron microscope housed at the John de Laeter Centre (JdLC), Curtin University, Perth, Australia, and included electron backscatter diffraction (EBSD) and energy-dispersive X-ray spectroscopy (EDS) mapping. Analyses were undertaken with an accelerating voltage of 20 kV and an instrument-specific “beam intensity” of 17 using a working distance of 20 mm and 70° specimen tilt. For mapping of rutile, a 500 nm step size was used, and the match units for rutile were obtained from the American Mineralogist Crystal Structure Database (801 448-45x) (Swope et al. 1995). Match units for monazite were derived from the crystallographic data of Ni et al. (1995), following Erickson et al. (2015). EBSD mapping of the monazite inclusions was done using a 50 nm step size. Post-processing of EBSD data was performed in Matlab, version R2022b, with the free toolbox MTEX Version 5.8.2 (Bachmann et al. 2010). Images were constructed using local misorientation and the mean misorientation of the rutile grain. The maps were plotted using the “roma” scientific color map (Crameri 2018). Post-processing involved noise-reduction by removal of groups of <5 adjacent pixels (“Wild” spikes/shards) with crystal orientations within 10° of those of their neighbors. The procedure was followed by applying a  $5 \times 5$  pixel median filter. The filter smooths the orientations in the EBSD data while preserving subgrain boundaries. Slip system characterization was undertaken following established methodologies (Lloyd et al. 1997; Prior et al. 2002; Reddy et al. 2007).

### Focused ion beam SEM and TEM

Analysis by transmission electron microscopy (TEM) and atom probe tomography (APT) requires samples to be prepared in the form of electron-transparent thin foils (TEM) or needle-shaped specimens (APT). These samples were prepared at two different institutes.

**Curtin University.** TEM and APT specimens analyzed at Curtin University were prepared on a Tescan Lyra3 Ga focused ion beam scanning electron microscope (FIB-SEM), housed in the John de Laeter Centre, Curtin University. The Tescan Lyra3 comes equipped with an electronically operated nanomanipulator

and Pt gas injection system. The FIB was operated with an accelerating voltage of 30 kV for the monoisotopic (mass 69 Da) Ga<sup>+</sup>-source. For backscatter electron (BSE) imaging in SEM mode, an accelerating voltage of the electron beam was varied between 5, 10, and 20 kV to provide a depth control on the size of the monazite inclusions below the surface. All TEM and APT specimens were extracted from one out of the two grains that contained monazite inclusions.

The TEM foil was prepared by cutting a vertical slice using the FIB and lifting it out using the nanomanipulator. The TEM foil was mounted on a copper half-grid and thinned until electron transparent (<100 nm), followed by a 2 kV clean-up routine to remove damage and Ga implantation caused by the 30 kV ion beam. After initial imaging by TEM, the sample was further thinned to 30–50 nm to reduce the curvature effect of the inclusion during scanning TEM (S/TEM) EDS.

**Jean Monnet University (UJM).** One TEM foil was prepared using a Thermo Fisher Scientific FEI 125 Helios Nanolab 600i FIB-SEM hosted by the MANUTECH USD platform in Saint-Etienne (France). Before extraction of the sample, the area of interest is protected with a 1 µm carbon coat. A 30 kV, 10 nA Ga-ion beam is used to cut out the foil ( $15 \times 10 \times 1$  µm). The foil is then lifted out and deposited on a Cu half-grid, thinned with an ion beam until ~100 nm thickness, and then “cleaned up” at low voltage (2 kV) to remove the amorphous part, resulting in a sample ~60 nm thick.

### Transmission electron microscopy (TEM)

TEM analysis at Curtin University was performed on the FEI Talos FS200X field emission gun TEM equipped with a Super-X EDS detector housed in the John de Laeter Centre. The TEM was operated at 200 kV. TEM imaging was conducted in both bright- and dark-field (BF and DF) modes. The TEM diffraction investigation was conducted with the assistance of Kikuchi patterns that were generated with the convergent beam electron diffraction (CBED). A small spot was used to minimize the beam-related damage to the sample, and the sample was tilted to the right diffraction zone axis or two-beam condition to acquire selected-area diffraction (SAD) patterns. Both BF and DF TEM imaging were undertaken with the objective apertures after tilting the sample to a diffraction condition within 20° of horizontal. TEM, STEM, and EDS data acquisition were conducted with the Velox software.

Chemical analysis was done by two pairs of attached super X detectors. The TEM is fitted with four scanning transmission electron microscopy (STEM) detection systems: high-angle annular dark-field (HAADF), upper dark-field (DF4), lower dark-field (DF2), and bright-field (BF). The contrast in HAADF is predominantly made from chemical/phase differences, and the contrast in BF is predominantly made from orientation differences. The DF4 and DF2 detectors reveal both chemical and orientation contrasts at different levels. HAADF TEM images provide information based on atomic number (Z) contrast with high-Z values being brighter. EDS data was acquired with a beam current of 0.6 nA and collected over 45–90 min for each presented map.

TEM characterization in UJM Saint-Etienne was performed with a Cs-corrected TEM (NeoARM200F Cold FEG) operated at 200 kV, operated by the Consortium Lyon Saint-Etienne de Microscopie (CLYM) and hosted within the Hubert Curien Laboratory. The instrument is equipped with a wide-angle energy-dispersive X-ray (EDX) spectrometer, SDD CENTURIO-X, from JEOL, two STEM detectors (annular dark-field and annular bright-field from JEOL and Gatan) with a CMOS camera Gatan Rio (4k×4k), a CCD camera Ultrascan from Gatan (2k×2k), and an electron energy loss spectrometer (EELS) (Gatan GIF Quantum ER). The resolution in STEM at 200 kV is 0.78 Å due to the presence of a Cs corrector CEOS ASCOR.

### Sample preparation for atom probe tomography (APT)

For the preparation of APT specimens, monazite was marked by depositing Pt buttons in the middle of the targeted inclusion prior to the deposition of a protective layer (Rickard et al. 2020). APT specimen preparation followed lift-out and sharpening procedures described elsewhere (Rickard et al. 2020; Thompson et al. 2007). A wedge-shaped sample was cut using the ion beam at an angled surface and lifted out using a nanomanipulator. The wedge was brought to the APT specimen holder consisting of a coupon with 22 silicon posts to hold the specimens. The wedge was aligned over the top of a silicon post, and a segment was attached using ion beam deposition with a Pt precursor. The wedge above the post was cut, leaving  $\pm 2$  µm of sample on the silicon post. This process is repeated until all material in the wedge has been placed on the posts. Following the mounting of specimens on the silicon posts, the specimens were then sharpened using an annular milling technique until needle-shaped specimens ~2.5 µm in length and <100 nm wide at the tip were formed. This was followed by a 2 kV clean-up routine to remove

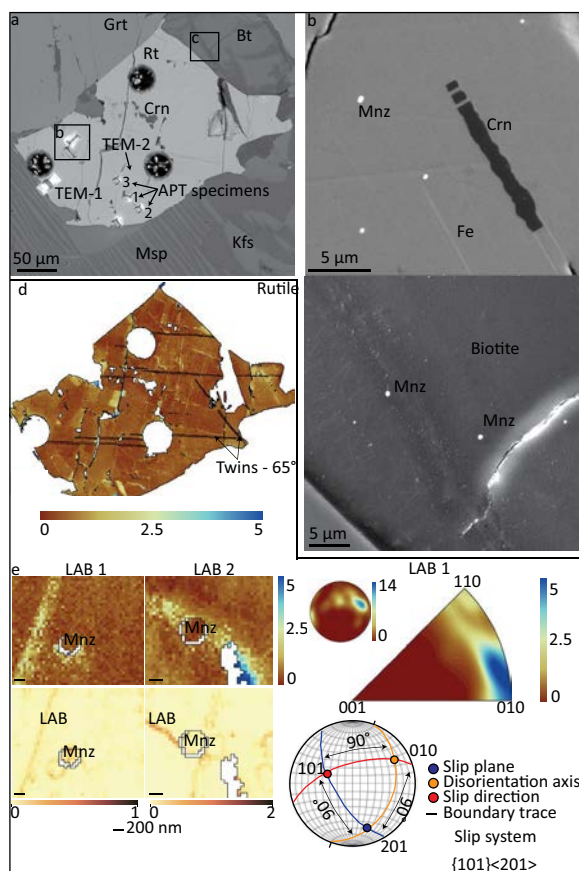


**FIGURE 2.** (a) BSE images of analyzed rutile (Rt). Rutile is surrounded garnet (Grt), mesoperthite (Msp), K-feldspar (Kfs), and biotite (Bt). The lift-out locations for TEM and APT specimens are indicated on the image. TEM-1 corresponds to the lift-out taken at Curtin University and this monazite has a recrystallized rim. TEM-2 corresponds with the monazite that does not show the recrystallized rim. (b) BSE image showing the presence of the submicrometer monazites (Mnz) in rutile, as well as corundum (Crn) and Fe-oxide exsolutions. (c) BSE image of biotite directly in contact with rutile, also hosting submicrometer monazite. (d) Mean-misorientation map showing the subtle differences in orientations that are linked to low-angle boundaries. The black boundaries show the location of twin boundaries (cf. Verberne et al. 2022). (e) Mean-misorientation and local misorientation maps for two low-angle boundaries. In both maps a monazite is present, with LAB 1 being in close vicinity and LAB 2 being pinned on the monazite inclusion. The corresponding slip system for the low-angle boundaries is  $\{101\} \langle 201 \rangle$ . (Color online.)

the damaged layer. All specimens were imaged by secondary electron (SE) and backscatter electron imaging (BSE) imaging in SEM-mode only at a working distance of 6 mm and an accelerating voltage of 10 kV.

### Atom probe tomography (APT)

APT analyses were conducted at the Geoscience Atom Probe Facility, Curtin University. This system is a Cameca Local Electrode Atom Probe (LEAP) 4000X HR that allows laser-assisted field evaporation and high mass-resolving power. Data were collected using a 125 kHz pulse rate, a laser pulse energy of 100 pJ, a base temperature of 70 K, and an ion detection rate of 0.3% based on Fougereuse et al. (2018) and Verberne et al. (2019). Post-processing was done using Cameca's Integrated Visualization and Analysis Software (IVAS) 3.8.0. Reconstructions are

based on the density of rutile and using the shank-angle reconstruction mode because of the poly-phased nature of our region of interest (Fougereuse et al. 2021c).

Atoms are evaporated as both single ions and molecular species with a range of different ionization states. Peaks in the mass spectra were labeled per individual isotope for specific ionization states and ranged with a constant width of 0.2 Da. For visualization and compositional analyses, isoconcentration surfaces (Hellman et al. 2000) were computed in IVAS using 1–2 at% for the respective element of interest. These isoconcentration surfaces can be used to isolate each of the individual phases in the data sets. System details, reconstruction parameters and other experimental conditions are summarized in Online Materials<sup>1</sup> DR-1 following the recommendation of Blum et al. (2018a).  $^{207}\text{Pb}/^{206}\text{Pb}$  ratios are calculated with corrections for background levels and thermal tails. Pb in these samples can be detected at two different ionization states,  $\text{Pb}^+$  and  $\text{Pb}^{++}$ , and corrections are needed to account for the  $^{206}\text{Pb}^{++}$  (103 Da) peak tail on the  $^{207}\text{Pb}^{++}$  (103.5 Da) peak, but also  $\text{P}_2\text{O}_5$  (205 Da) on  $^{206}\text{Pb}^+$  (206 Da) and  $^{206}\text{Pb}^+$  (206 Da) on  $^{207}\text{Pb}^+$  (207 Da). Measurement of isotopic ratios was undertaken using a range of different peak widths and bin sizes following Blum et al. (2018b).

From the prepared submicrometer monazite specimens ( $n = 11$ ), APT analysis resulted in three successful runs, with a respective yield of 70, 45, and 9 million detected ions. The analysis of interfaces provides a challenge as the interface is a weak spot in the material. The 3D reconstructions show that in all specimens, the monazite is encapsulated within rutile, indicating that only the rim of the monazite inclusions was analyzed. Monazites not encapsulated by rutile in the APT specimen likely delaminated during the analysis. The data sets were evaluated by generating isoconcentration surfaces that subdivide the specimens into three components—rutile, monazite, and the interface. This allowed for the separate interpretation of the mass spectra of each component.

## RESULTS

### Petrography and analysis of the rutile host

The studied rutile grain occurs in a rock consisting of residual layers and leucosomes. Monazite inclusions are found in two rutile grains within this thin section, as well as in the directly surrounding biotite (Figs. 2b–2c). No monazite inclusions were found in the garnet or mesoperthite. The rutile grain studied is  $\sim 250 \times 200 \mu\text{m}$  in size, with at least 46 sub-micrometer monazite inclusions visible at the surface. EBSD mapping of individual monazite grains shows no evidence for a crystallographically preferred orientation of the inclusions in either the rutile or the surrounding biotite (Fig. 2d).

Several different microstructures are revealed by EBSD mapping. Twin boundaries are observed in two orientations corresponding to a  $65^\circ$  rotation and belong to the  $\{101\} \langle 100 \rangle$  twin relationship. In addition, a network of low-angle boundaries (LAB) (see Figs. 2d–2e) is visible. The low-angle boundaries have a misorientation axis of (010), with the dispersion of  $1\text{--}2^\circ$ , corresponding to the  $\{101\} \langle 201 \rangle$  slip system (Fig. 2e). The LAB are straight (LAB 1) or bent around the monazite inclusions (LAB 2).

**Atom probe observations of the rutile host.** Fe and Zr, which are common trace elements in rutile, are detected within the mass spectra. U and Pb are not observed above the background (Fig. 6). In the 3D reconstruction, no heterogeneities can be observed within the rutile matrix this includes ranging the theoretical U and Pb peaks. The rutile mass spectra are comparable to those obtained during previous APT studies of rutile (e.g., Verberne et al. 2019, 2023).

### Structural and chemical analysis of the monazite inclusions

The examination of two TEM thin foils, both incorporating a single monazite inclusion, indicates variations in the texture and chemical associations of the outer rim of monazite in the two



inclusions. In one monazite, there is a clear core-rim structure (Fig. 3). In contrast, the second monazite inclusion only records the “core” structure throughout the entire inclusion (Fig. 4). In both monazites, the core has a high density of clusters, while the rim structure has a lower density of clusters but this records a discrete compositional variation (Figs. 4 and 5)

Trace elements observed within the monazite APT mass spectra (Fig. 6) include  $\text{Ca}^{++}$  (20 Da),  $\text{Mg}^{+}$  (24 Da), and  $\text{Li}^{+}$  (6 Da).  $^{238}\text{U}$  was detected as  $^{238}\text{UO}_2^{++}$  at 135 Da, and no peak was present for  $^{235}\text{UO}_2^{++}$ . Pb in monazite is observed with two different ionization states:  $^{206}\text{Pb}^{+}$  and  $^{207}\text{Pb}^{+}$  (206 and 207 Da) as well as  $^{206}\text{Pb}^{++}$  and  $^{207}\text{Pb}^{++}$  (103 and 103.5 Da).  $^{208}\text{Pb}^{+}$  and  $^{208}\text{Pb}^{++}$  were not observed above the background. Furthermore, no Th-bearing species were identified within the mass spectrum.

**Chemical heterogeneities in the monazite core.** The inner region of the monazite exhibits a mottled texture identifiable in BF mode (Fig. 4). In one monazite, this texture is only present in the core region, whereas this texture is present throughout the second monazite grain imaged by TEM. The mottled texture is due to the presence of dark (in BF mode) and bright (in DF mode) spots. These reflect radiation damage and crystal defects as well as nanoclusters  $\pm 5$  nm in size. STEM-EDS revealed some of these nanoclusters are composed of trace elements (U, Pb, and Ca) (Figs. 7a–7b).

**Trace element distribution in the monazite rim.** This rim is only visible in one of the two imaged monazites (Fig. 4b). The monazite rim is  $\sim 100$  nm wide. Here, the matrix of the monazite appears pristine while hosting several nanoclusters 20–30 nm in diameter (Fig. 5). Lattice imaging of the clusters shows a continuous lattice consistent with monazite (Figs. 5d–5f). Here, we differentiate between a cluster and inclusion based on similar properties as mentioned in Turuani et al. (2023). The presence of a grain boundary is indicative of an inclusion, whereas a continuous lattice/absence of a grain boundary is an indication of a cluster. The clusters in the monazite consist of two types of darker clusters, as seen in the HAADF images (Figs. 4b, 7c, and 7d), and sometimes encompass one or two bright spots. One type of darker cluster was shown to be rich in Ca (Fig. 7c). However, the second type of nanocluster did not yield an EDS response. This indicates the major constituents of this cluster may have an atomic number that is too low for S/TEM-EDS ( $Z = 6$ ). Alternatively, this could point to a void and represent porosity within the cluster. The bright spots within both these clusters yielded an increased concentration of Pb (Fig. 7c).

The 3D reconstruction of the monazite APT reveals two types of clusters in the monazite rim (Fig. 8). The first type is dominated by Ca. These clusters have a diameter of 20–30 nm

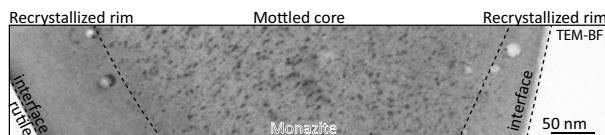


**FIGURE 3.** TEM BF cross section to illustrate the structure of the monazite inclusion. From outward inward: the rutile host; the interface between rutile and the monazite; the recrystallized rim including 5–20 nm clusters and nano-inclusions of Li, Ca, and Pb; and the core of the monazite exhibiting a mottled texture.

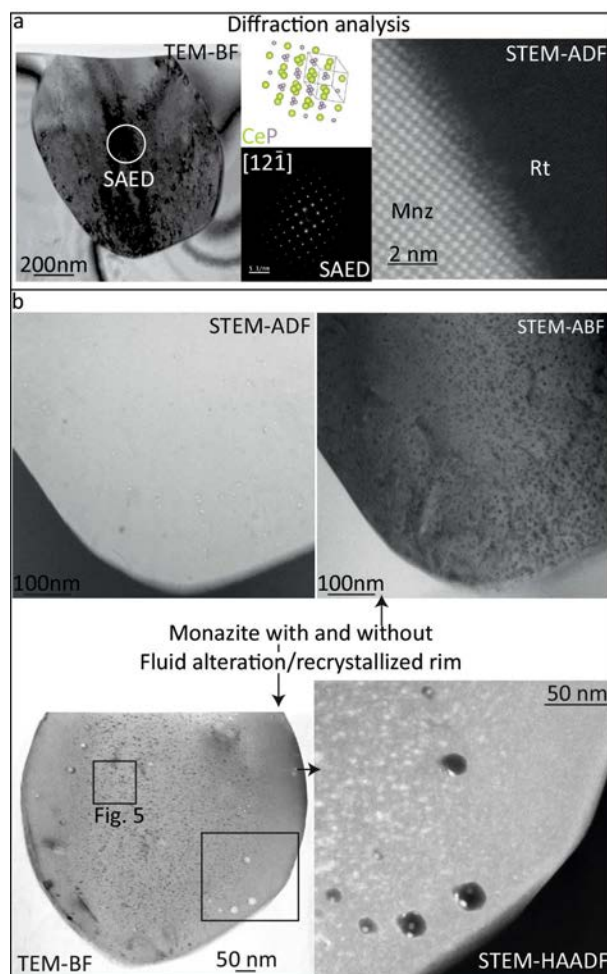


**FIGURE 4.** TEM/STEM characterization of the TEM foils. (a) From the left to the right: TEM-bright field (BF) image of one entire monazite inclusion in rutile; selected-area electron diffraction (SAED) pattern from the monazite inclusion seen in the  $[12\bar{1}]$  zone axis and associated with a crystallographic model from  $\text{CePO}_4$ -monazite in the same orientation and high-resolution STEM-annular dark-field (ADF) image of the monazite-rutile interface. (b) top) Left STEM-ADF and right STEM-ABF images from part of the Mnz inclusion are seen in a. (b) bottom) STEM BF and HAADF images from a Mnz inclusion with an alteration rim. (Color online.)

containing up to 10 at% Ca (Fig. 9). Ca-rich inclusions are often accompanied by an increase in Pb of up to 2–3 at% as well as Y, up to 1.2 at%. However, not all Ca-rich inclusions show an increase in the Pb signal. The increase in Ca and other trace elements is compensated by a depletion in REE and O, with P remaining relatively constant. Pb is spread over four peaks within the mass spectrum, resulting in insufficient counts for meaningful determination of  $^{207}\text{Pb}/^{206}\text{Pb}$  ratios after correcting for the static background and the tails of the preceding peaks. Therefore, despite the presence of Pb within the inclusion, no isotopic composition could be obtained.

The second inclusion type is enriched in  $\text{Li}^{+}$ , with values up to 30 at% Li (Fig. 9). These inclusions are  $\sim 20$  nm in diameter.

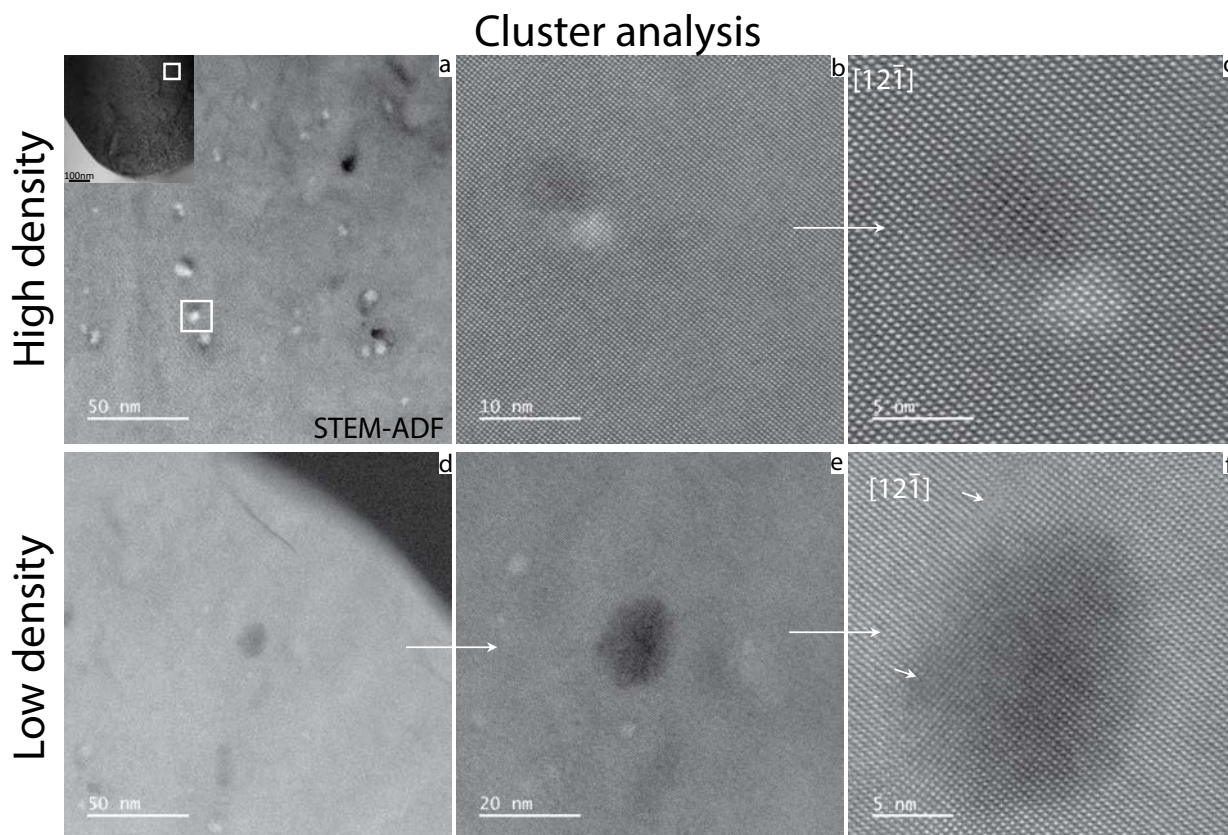


**FIGURE 5.** STEM-ADF images of clusters in the core and recrystallization rim. (a–c) within the core there is a high density of clusters (bright spots), which are trapped within zones of radiation damage (black spots). (d–f) The recrystallized rim yields far fewer bright spots; however, different inclusions are visible. Note that despite the presence of clusters and inclusions, the lattice is almost not affected.

Li-rich inclusions have Pb concentrations up to 0.6 at% and, therefore, incorporate less Pb than the Ca-rich inclusion, yet have elevated levels compared to the monazite matrix. Like the Ca-rich inclusions, the increase of Li and other trace elements is compensated by a depletion in REE and O, with P remaining at roughly 10 at%. (Fig. 9). Pb isotopic compositions could not be obtained from the Li-inclusions for similar reasons as with the Ca-inclusions.

#### The rutile-monazite interface

The interface between rutile and monazite inclusion is sharp and coherent (Fig. 4a). Chemical mapping of the interface by TEM shows the enriched zone in the interface between the rutile and monazite is ~2 nm wide at the narrowest part of this boundary.

STEM-EDS analysis was applied to further characterize the different features present within the monazite. The interface between rutile and monazite with core-rim texture yields 2–4 at% Pb based on a line profile across the interface (Fig. 7d) and with no signals above the detection limit for other trace elements.

The mass spectra obtained from the interface show components of both the monazite and rutile mass spectrum. The boundary is enriched in trace elements, including U, Pb, Ca, Li, Mg, Si, and Al. Ca and Pb concentrations reach 2–3 at% in all three specimens. The trace element distribution at the interface of specimen 3 is heterogeneous, most clear for trace elements

with a lower overall concentration, e.g., Si and Al (Fig. 10), but similar distributions can be observed for Pb (Fig. 10).

The heterogeneous distribution of trace elements in the interface of specimen 3 is visualized in the reconstruction and measured along a 1D profile (Fig. 10). The combined concentrations of Al + Si are shown, and contrast in concentration is visible from the apex of the tip to the lower part of the reconstructed volume. The transition from low to higher concentration is accompanied by linear features enriched (labeled A, B, and C) in trace elements. Additionally, clusters of Mg are present at this interface. These clusters contain up to 20 at% Mg and have a Ca concentration of ~4 at% (Fig. 9), which is higher than the average concentration within the interface. The width of the interface was estimated to be ~8 nm based on the Pb concentration profile.

#### Pb isotopic compositions of interfacially segregated Pb

The APT mass spectra of the interface between rutile and monazite show  $^{206}\text{Pb}$  and  $^{207}\text{Pb}$  are present as both  $\text{Pb}^+$  and  $\text{Pb}^{++}$ . The 3D reconstruction shows the Pb is homogeneously distributed along the interface of specimens 1 and 2 and heterogeneously in specimen 3 (Fig. 10). Pb isotopic signals were retrieved from the interfaces of all three specimens. The background- and thermal-peak-tails-corrected  $^{207}\text{Pb}/^{206}\text{Pb}$  ratios are  $0.0900 \pm 0.0198$  ( $2\sigma$ ) for specimen 1,  $0.1016 \pm 0.0224$  ( $2\sigma$ ) for specimen 2, and  $0.1733 \pm 0.0156$  ( $2\sigma$ ) in specimen 3. Hence, the

Pb isotopic signals and calculated  $^{207}\text{Pb}/^{206}\text{Pb}$  ratios for specimens 1 and 2 are identical within error. Specimen 3, however, yields a higher ratio. Calculated model ages for, respectively, specimens 1, 2, and 3 are  $1370 \pm 420$  Ma ( $2\sigma$ ),  $1590 \pm 420$  Ma ( $2\sigma$ ), and  $2580 \pm 150$  Ma ( $2\sigma$ ). U in the interface was detected as  $^{238}\text{UO}_2^{++}$ . The concentration of U compared to Pb is very low, with a  $^{238}\text{U}/^{206}\text{Pb}$  ratio of  $<0.04$  in all three specimens. Therefore, it is expected the influence on the  $^{207}\text{Pb}/^{206}\text{Pb}$  ratio is negligible.

## DISCUSSION

### Monazite inclusions in rutile

Inclusions typically occur either as a product of exsolution or incorporation during growth. In the rutile studied here, exsolution is unlikely since monazite is present in different host phases (rutile and biotite). The monazite lacks a crystallographically preferred orientation that is expected when monazite forms via an exsolution mechanism. Furthermore, P and REE concentrations in rutile are typically very low, with any significant amounts of REE only reported in extraterrestrial Niobian-rutile ( $>6$  wt%  $\text{Nb}_2\text{O}_5$ ) (Hlava et al. 1972). Therefore, the monazites are interpreted to be primary inclusions trapped within the rutile.

The encapsulation of monazite within rutile potentially shields the monazite from external processes (Daneu et al. 2014; Hart et al. 2016, 2018). However, the measured Pb isotopic compositions of monazite at inclusion interfaces are different. The rutile host is characterized by the presence of several twin boundaries and LABs, and these could aid in the diffusion of

elements in rutile (Verberne et al. 2022). As shown, some monazite inclusions are in direct contact with these LAB's (Fig. 2). Potentially, these inclusions would no longer be fully shielded, and trace elements are able to migrate out of the rutile-monazite interface. Depending on the timing, inclusions within a single rutile grain could record different isotopic signatures.

### Formation of trace-element enriched nanoscale clusters

**Nanoclusters in the monazite core.** The two types of monazite inclusions are: one with a mottled texture due to radiation damage and one with a distinct core-rim structure (Figs. 4 and 5). S/TEM EDS shows that some of the dark and bright spots that lead to the mottled texture are enrichment in Ca, U, and Pb (Fig. 7). The texture and formation of trace-element-enriched clusters are explained via entrapment in defects generated via radiation damage (Seydoux-Guillaume et al. 2018, 2019). The damaged regions stand out due to structural differences with the host monazite, while the bright spot (HAADF) stands out due to being enriched in trace elements, creating this mottled texture as previously observed by others (Seydoux-Guillaume et al. 2019; Turuani et al. 2022, 2023).

Clusters within a matrix typically represent a low-energy configuration and are preferable sites for trace elements compared to the crystal lattice of the host. With the rutile present during UHT metamorphism at 2580 Ma (Clark et al. 2019), the temperature conditions are met for Pb diffusion into clusters (as observed in Seydoux-Guillaume et al. 2019).

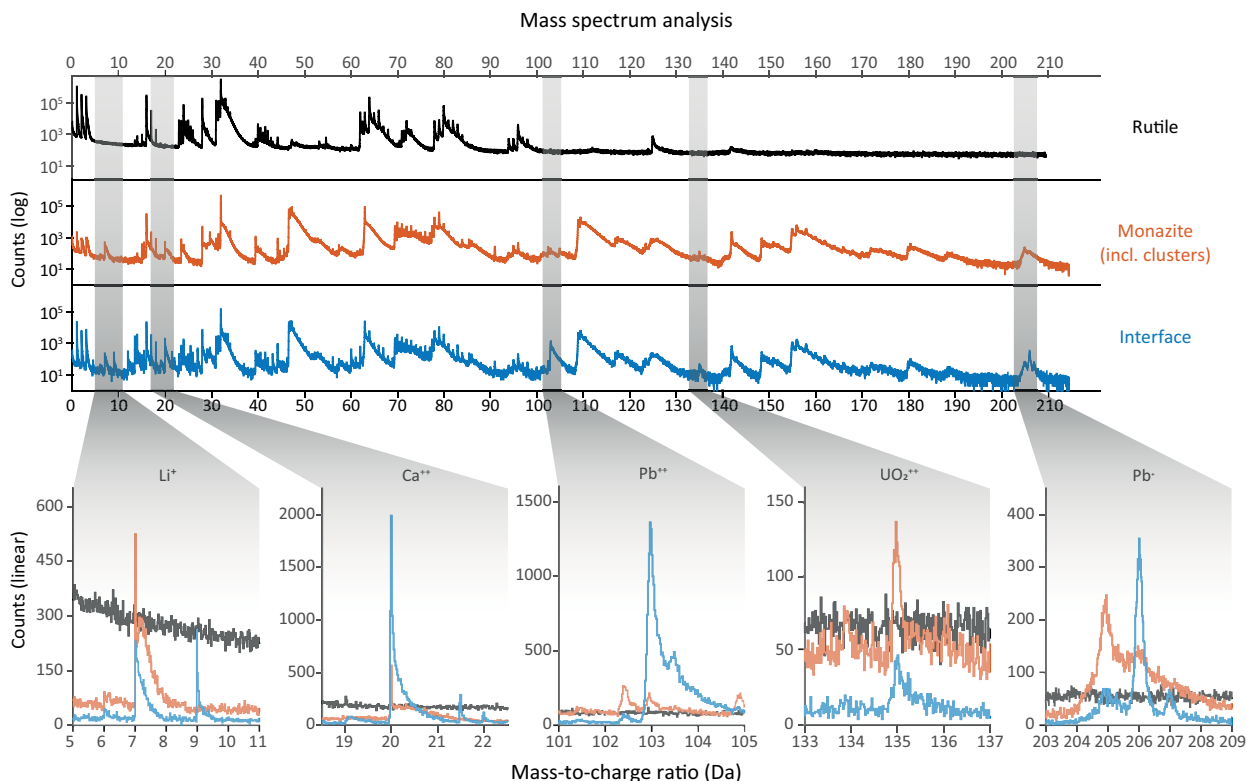


**FIGURE 6.** Mass spectrum of rutile, monazite and the interface with highlighted trace elements that are enriched in the interface. Li, Ca, and U are observed in one location in the mass spectrum. Pb is observed at both  $\text{Pb}^+$  and  $\text{Pb}^{++}$ .  $^{206}\text{Pb}$  is visible at 103 Da and 206 Da, and  $^{207}\text{Pb}$  is observed at 103.5 Da and 207 Da.  $^{208}\text{Pb}$  is not present above background. (Color online.)



The mottled texture, therefore, is the result of an interplay between the formation and healing of radiation damage sites and the capture of trace elements in these sites during high-temperature events, which allow for more rapid diffusion of elements.

**Nanoscale clusters in the monazite rim.** The rim hosts Ca-rich and Li-rich nanoscale clusters. Given that the lattice of the Ca-rich cluster is the same as the host monazite (Fig. 5) with relatively high-REE concentrations, these clusters are interpreted to be a solid solution within monazite rather than represent a separate phase.

The Li-rich nanoscale cluster has low-REE concentrations (<4 at%) with Li concentrations between 24 to 30 at% and P

concentrations of  $\pm 10$  at% (Fig. 9). In the literature, we found no reference to the formation of Li-phosphate in monazite. Nevertheless, the composition of the Li-rich cluster may indicate the formation of a separate Li-phosphate phase.

The Mg-rich clusters are only present within the interface and consist of 20 at% Mg, 10 at% P, and 4 at% Ca, while showing a depletion in REE concentrations compared to the monazite host. As is the case for the Li-phosphate cluster, the high concentration of Mg suggests the formation of a new phase via a similar mechanism to the formation of the Ca- and Li-phosphate clusters.

**Pb-rich nanoclusters.** Bright spots in HAADF mode associated with the Ca- and Li-rich clusters are rich in Pb based

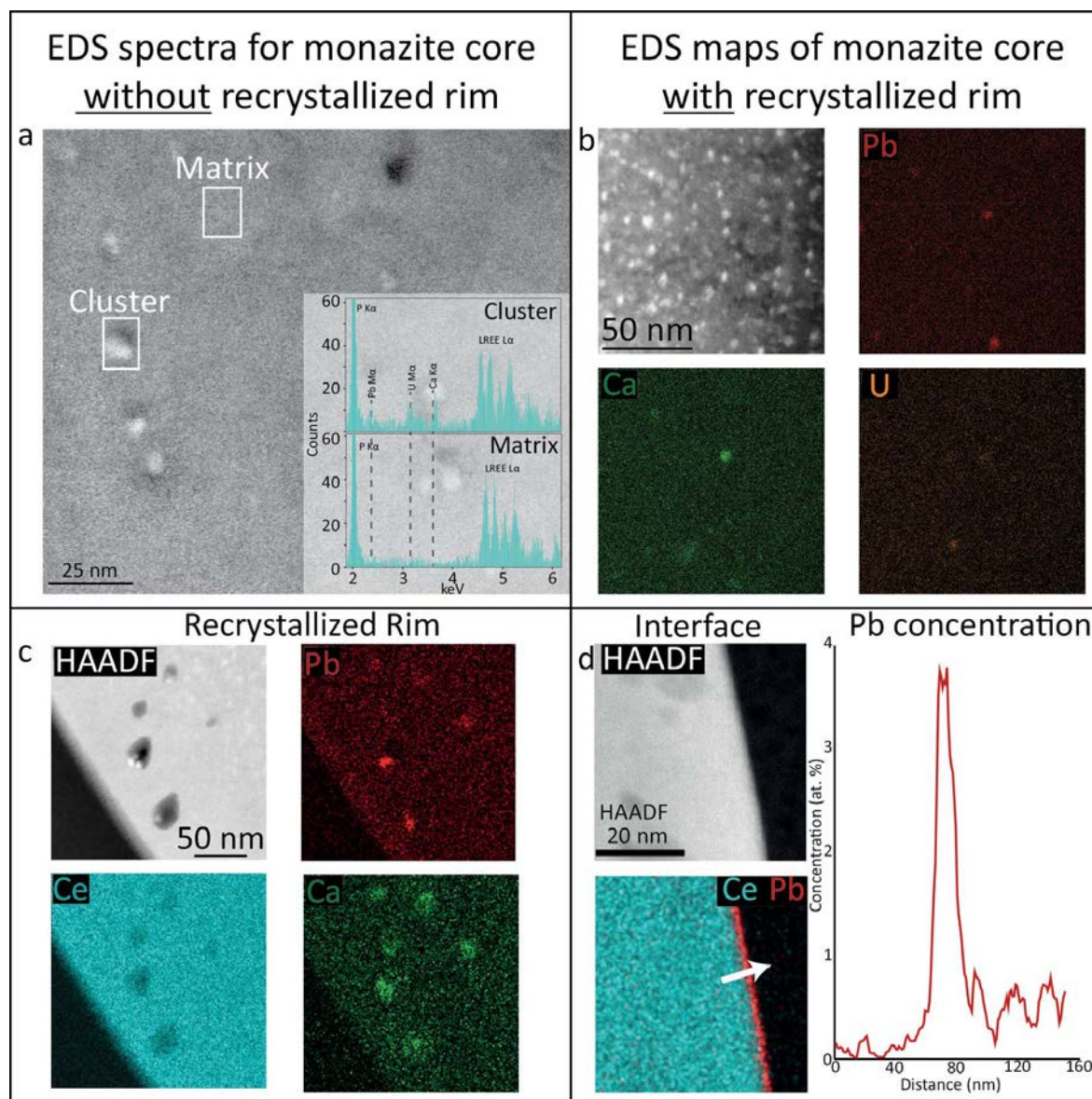


**FIGURE 7.** TEM EDS spectra and maps. (a) TEM EDS analyses were conducted on a monazite without a recrystallized rim. EDS analyses were performed on the matrix and a cluster to show the difference in composition and the presence of Ca, Pb, and U in the cluster. (b) TEM EDS maps of the core of the monazite with a recrystallized rim showing the clusters are rich in Ca, Pb, and U. (c) TEM EDS maps of clusters present in the recrystallized rim. Ce is shown as an indication for decreased concentrations of major elements. (d) TEM EDS interface analysis, showing an EDS map to highlight that Pb is enriched at the interface with a Pb concentration profile (white arrow). (Color online.)



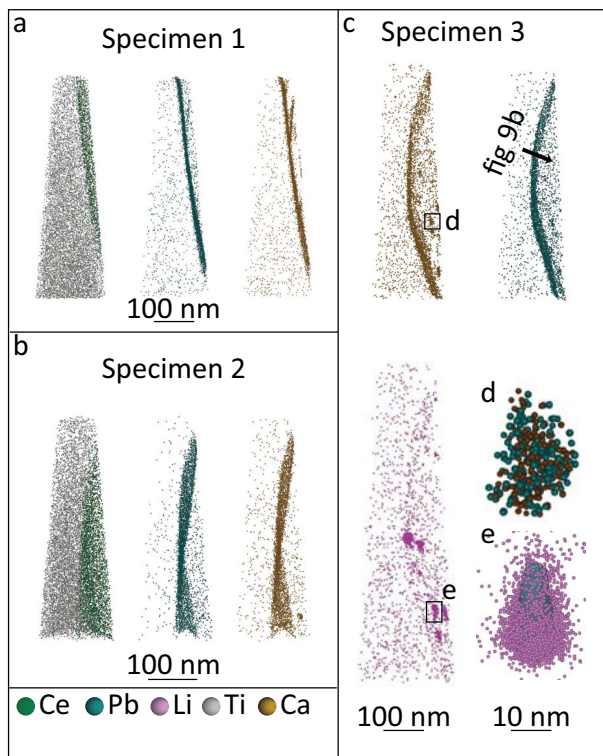


**FIGURE 8.** (a and b) Ion maps of specimens 1 and 2 showing monazite (green) is encapsulated within rutile (gray). The interface is enriched in Ca and Pb in both specimens. Also, the curvature over the monazite interface is clearly visible in the ion maps of specimen 2. (c) Ion maps of specimen 3 not only yields a Pb and Ca enriched interface but also reveal the presence of Ca (d) and Li-rich (e) inclusions. Within the Li-rich inclusion an isoconcentration surface for Pb is shown to demonstrate the presence and equivalence of the inclusions in Figure 4b. (Color online.)

on STEM-EDS (Fig. 7). Furthermore, the APT based proximity histogram of the Ca- and Li-rich cluster also shows elevated values of Pb. The lack of  $^{204}\text{Pb}$  and  $^{208}\text{Pb}$  signals indicated there is no-to-negligible  $^{232}\text{Th}$  or common Pb component. Potentially, these Pb-rich nanoclusters reflect the same clusters observed within the monazite core. The Pb nanocrystals within the Ca- and Li-phosphate cluster have the same general appearance as Pb present in a Si-rich cluster recently described in zircon by other studies (Kusiak et al. 2015, 2019; Lyon et al. 2019), called nanospheres, and monazite (Turuani et al. 2022, 2023) referred to as nanocrystals. Considering we observe a similar presence of Pb in the core that is associated with U decay, it is unlikely these are primary Pb phases. Furthermore, since we lack data on the structure or valence state of the Pb and associate the Pb with U decay, these Pb-rich particles do not fall within the definition of metallic Pb nanospheres (Kusiak et al. 2015, 2023).

These Pb-rich nanocrystals are intimately linked to the Ca, and Li-rich phosphate clusters, which raises questions about the timing of their formation. One possibility is concurrent formation, with Ca, Li, and Pb migrating at the same time. However, this seems unlikely, as the Pb-rich nanocrystals in the monazite rim are not observed outside of the Ca and Li-rich clusters. If the Pb-rich nanocrystals are indeed the same as those in the core this

indicates that during the formation of the rim and the Ca- and Li-rich clusters, the Pb nanocrystals become trapped, preventing small volumes of Pb migrating toward the interface.

#### A Pb mobility model

The texture and compositional variations of the submicrometer monazite inclusions in rutile provide insight into the tectonothermal history of the studied sample. First, the mottled texture of the monazite (core) is ascribed to both a combination of the presence of radiation damage and the segregation of trace elements into those radiation defects leading to the formation of nanoscale clusters (Seydoux-Guillaume et al. 2002a, 2004, 2018, 2019; Turuani et al. 2023). Depending on the time of monazite growth and the diffusion of trace elements into defects the clusters rich in Pb can be dated if enough time has passed to accumulate radiogenic Pb. This diffusion process is the first stage of trace element mobility.

Second, in some of the monazite crystals, the rim yields a different distribution of clusters. The texture indicates partial recrystallization of the monazite rim and encompasses Ca- and Li-phosphate clusters as well as Pb-rich nanocrystals. The presence of a recrystallized rim in only some of the monazite crystals shows that the reaction is localized.

Rutile and other repository minerals preserve inclusions due to their low compressibility (Mosenfelder et al. 2005). When exhumed, rutile exerts an overpressure on inclusions (Hart et al. 2016). Differences in compressibility between the rutile host and the inclusions will result in stress acting upon the monazite

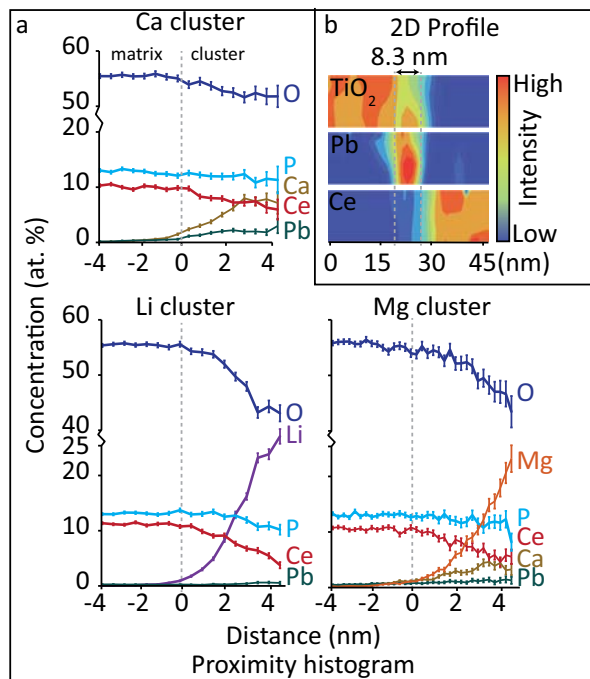


**FIGURE 9.** (a) Proximity histograms for the three inclusions observed within the APT data. All inclusions show a slight increase in Pb concentration and a strong increase in one of three cations (Ca, Li, Mg), indicating the formation of a new phase or solid-solution. Ce is shown as a proxy for the REE, which shows similar trends at lower concentrations. (Color online.)

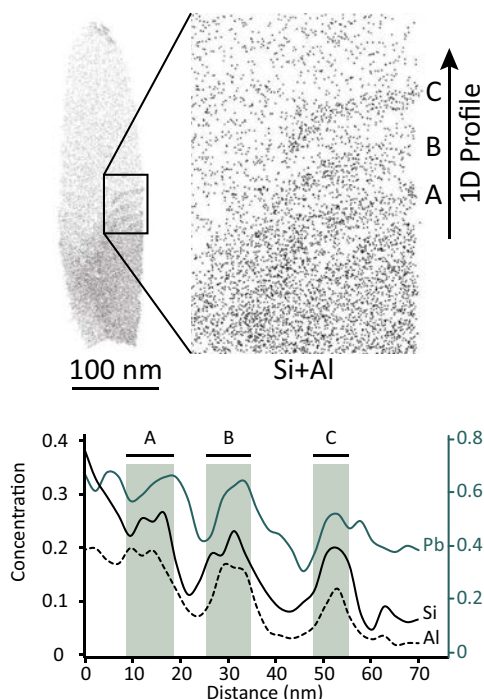


**FIGURE 10.** Ion map showing the heterogeneous distribution of Si + Al within the interface of specimen 3. The 1D concentration profile was taken along the interface, as indicated in the top panel. The enrichment of Al, Si, and Pb clearly varies within each section. The linear features near the middle are interpreted as dislocation present at the interface. (Color online.)

(Huang et al. 2010; Zaffiro et al. 2019). Therefore, one explanation could be that the formation of the rim in the monazite is the result of localized stress-induced recrystallization. Alternatively, the presence of Li, and to a lesser extent Mg, could indicate infiltration of a fluid. This, too, could cause recrystallization of the monazite rim. In general, rutile is resistant to the infiltration of fluids (Triebold et al. 2007; Zack et al. 2004b). As argued in recent studies on the nanoscale and microstructures in rutile (Verberne et al. 2022, 2023), the presence of twin boundaries and low-angle boundaries could allow for the transport of trace elements. The same structures potentially facilitate fluid infiltration as well. However, we observe Li primarily in clusters and only minor concentrations in the interface itself. Therefore, a localized stress-induced recrystallization appears to fit better with these observations.

**Low-Th monazite.** The absence or very low concentration of Th in monazite is an odd observation as  $\text{ThO}_2$  concentrations in monazite are mostly reported to be between 1–12 wt% (e.g., Janots et al. 2012; Seydoux-Guillaume et al. 2018). However, a few studies report monazite with <1 wt% (e.g., Demartin et al. 1991; Mannucci et al. 1986). Yet, these studies still show measurable amounts of Th. Closest to our observations is a study by Janots et al. (2008). X-ray maps of monazite show a monazite with high Th in the core and a recrystallized rim with low, but not absent, Th concentrations. However the rim analyzed by Janots et al. (2008) is 10 mm wide compared to our 100 nm wide rim, and thus five orders of magnitude larger. The same underlying

principle, recrystallization, would offer an explanation. The recrystallization would have occurred at a low-metamorphic grade (Poitrasson et al. 1996; Janots et al. 2008), with Th concentration being positively related to the metamorphic grade (Seydoux-Guillaume 2002b). This supports our hypothesis of localized stress-induced recrystallization.

#### Trace element systematics at the rutile-monzazite interface

The distribution of trace elements at the interface between monazite and rutile in specimen 3 is heterogeneous (Fig. 10). In Figure 10, lower concentrations of trace elements are observed in the upper part of the boundary compared to the lower part of the boundary. The transition occurs across a domain with linear features rich in trace elements. These linear features are an expression of dislocations at the interface (Dubosq et al. 2019; Fougrouse et al. 2021b; Verberne et al. 2022, 2023). Heterogeneities at phase boundaries are commonly observed and well-studied within the material sciences (Larere et al. 1988; Sutton and Balluffi 1995; Suzuki et al. 1981, 1991). There is extensive evidence that the degree of trace element segregation has an inverse relationship with interplanar spacing (Sutton and Balluffi 1995). In iron alloys, it was found that P migrates to boundaries when this spacing decreases (Suzuki et al. 1981). Also, P and S have different degrees of segregation toward boundaries with different orientations in Ni (Larere et al. 1988), and it is apparent that trace elements segregate in different amounts as a function to disorientation in olivine (Tacchetto et al. 2021). The segregation into boundaries for ionic systems is more complex since charge compensation needs to be considered (Kliewer 1965; Sutton and Balluffi 1995). In  $\text{TiO}_2$ , Ikeda and Chiang (1993) and Ikeda et al. (1993) demonstrated differences in segregation based on the valence states of trace elements e.g.,  $\text{Al}^{3+}$  and  $\text{Nb}^{5+}$ , boundary type, and temperature. Here, the curvature of the interface results in a continuous change of opposing crystal faces. Consequently, the spacing between the two phases will vary. This change is reflected in the segregation of trace elements, causing differences in localized trace element concentrations.

#### IMPLICATIONS FOR GEOCHRONOLOGY: A GEOLOGICAL HISTORY FROM SUBMICROMETER MONAZITE INCLUSIONS

The presence of inclusions with a radiogenic component different from the host mineral can result in a mixed chemical and isotopic system (Fougrouse et al. 2018; Turuani et al. 2022). In this study, Pb is found to have segregated in multiple ways that might have occurred at different moments in time. The clusters still preserved within the monazite core are the result of the interplay between the formation of radiation damage,  $\alpha$ -healing (Seydoux-Guillaume et al. 2018), and volume diffusion (Seydoux-Guillaume et al. 2019). While recrystallization led to the segregation of Pb from the monazite rim into the rutile-monzazite interface. We observe that the recrystallization of the monazite rim is local and not pervasive throughout the rutile grain. Also, we see Pb-enriched nanocrystals trapped within clusters in the recrystallized rim. This localized recrystallization combined with trapping of Pb-enriched nanocrystals suggests the Pb-enriched features formation and recrystallization occurred in two stages, though without Pb isotopic information from these nanocrystals and the clusters in the core then the timing of these stages remains elusive.

Regardless, the mobility results in several Pb reservoirs with potentially unique Pb isotopic signatures that record the timing of their formation and the decoupling of the U-Pb system. In ideal situations, this Pb signature can be independently studied (Fougerouse et al. 2018; Peterman et al. 2016; Seydoux-Guillaume et al. 2019; Turuani et al. 2022; Valley et al. 2014; Verberne et al. 2020).

In this study, the only reservoir with a significant amount of Pb measurable by APT is the interface between rutile and monazite. Age determination in APT data are based on analyzing the  $^{207}\text{Pb}/^{206}\text{Pb}$  ratios to derive the timing of Pb segregation in contrast to a direct age. The assumption is that this ratio is preserved after segregation. This also means that the presence of U or Th compared to total Pb needs to be minimal. Important to note that any additional influx of radiogenic Pb derived from the same source material will obscure the determination of the first event. However, such an event could possibly also record the latter, preserving both (Taylor et al. 2023). In our results, the absence of  $^{204}\text{Pb}$  and  $^{208}\text{Pb}$  supports the assumption that no common Pb is present and thus, all Pb is of radiogenic origin (Peterman et al. 2016; Valley et al. 2014; Verberne et al. 2020). The U/Pb ratios in the boundary are  $<0.05$ . This indicates large amounts of Pb are unsupported and that there is negligible production of radiogenic Pb via continued U decay after the Pb migration into the rim.

The  $^{207}\text{Pb}/^{206}\text{Pb}$  ratio varied between the interfaces in the three APT specimens. The obtained ratios are  $0.0900 \pm 0.0198$  ( $2\sigma$ ) for specimen 1,  $0.1016 \pm 0.0224$  ( $2\sigma$ ) for specimen 2 and  $0.1733 \pm 0.0156$  ( $2\sigma$ ) in specimen 3. Specimens 1 and 2 have  $^{207}\text{Pb}/^{206}\text{Pb}$  ratios with large uncertainties, however, specimen 3 yields a more precise ratio which can be evaluated. Let us reiterate that the monazite is enclosed within rutile. Radiogenic Pb produced by radioactive decay of U and the Pb will be retained in monazite. Later metamorphic and recrystallization events will mobilize the Pb, isolating it from U. Thus, the  $^{207}\text{Pb}/^{206}\text{Pb}$  ratio at the time of Pb segregation is preserved. The rocks in the Napier Complex have a complex history. The oldest potential time of formation is suggested by Black et al. (1984), with monazite crystallization around 3070 Ma. If we assume an initial crystallization age of 3070 Ma, the current  $^{207}\text{Pb}/^{206}\text{Pb}$  of  $0.1733 \pm 0.0156$  ( $2\sigma$ ) indicates Pb production for a duration of 2580 Myr before segregation. This would correspond with the decoupling of U-Pb occurring around 550 Ma, which would match the late hydrothermal event in the area (Black et al. 1983). This shows that analyses of grain boundaries, which are often avoided during geochronological studies, can provide additional information about the geological history.

## ACKNOWLEDGMENTS AND FUNDING

The work was conducted within the Geoscience Atom Probe Facility at Curtin University. S.M.R. and D.W.S. acknowledge Australian Research Council support (DP210102625). The Consortium Lyon St-Etienne de Microscopie (CLyM) is thanked for access to the TEM NeoARM in Saint-Etienne (France). Stéphanie Reynaud (Université de Saint-Etienne, France) is thanked for her help with FIB sample preparation of one TEM foil. A.-M. Seydoux-Guillaume thanks the Centre National de la Recherche Scientifique, L'institut National des Sciences de l'Univers (CNRS INSU) for financial support. We also thank Leanne Staddon and an anonymous reviewer for their constructive feedback.

Conflict of interest declarations: The authors declare there are no conflicts of interest. All authors contributed to the study. Concept: Rick Verberne. Design: Rick Verberne, Steven Reddy. Sample: Chris Clark. Material preparation: Rick

Verberne, Denis Fougerouse, William Rickard, Anne-Magali Seydoux-Guillaume. Data collection: Rick Verberne, David Saxey, Steve Reddy, Zakaria Quadri, Anne-Magali Seydoux-Guillaume. Data analysis: Rick Verberne, Steve Reddy, Anne-Magali Seydoux-Guillaume. The first draft of the manuscript was written by Rick Verberne, with review and editing by Steven Reddy, Denis Fougerouse. All other authors commented on previous versions of the manuscript. All authors read and approved the final manuscript.

## REFERENCES CITED

- Bachmann, F., Hielscher, R., and Schaeben, H. (2010) Texture analysis with MTEX-free and open source software toolbox. *Solid State Phenomena*, 160, 63–68.
- Bingen, B. and Van Breemen, O. (1998) U-Pb monazite ages in amphibolite-to granulite-facies orthogneiss reflect hydrous mineral breakdown reactions: Sveconorwegian Province of SW Norway. *Contributions to Mineralogy and Petrology*, 132, 336–353, <https://doi.org/10.1007/s004100050428>.
- Black, L., James, P., and Harley, S. (1983) The geochronology, structure and metamorphism of early Archaean rocks at Fyfe Hills, Enderby Land, Antarctica. *Precambrian Research*, 21, 197–222, [https://doi.org/10.1016/0301-9268\(83\)90041-4](https://doi.org/10.1016/0301-9268(83)90041-4).
- Black, L.P., Fitzgerald, J.D., and Harley, S.L. (1984) Pb isotopic composition, colour, and microstructure of monazites from a polymetamorphic rock in Antarctica. *Contributions to Mineralogy and Petrology*, 85, 141–148, <https://doi.org/10.1007/BF00371704>.
- Black, L., Williams, I.S., and Compston, W. (1986) Four zircon ages from one rock: The history of a 3930 Ma-old granulite from Mount Sones, Enderby Land, Antarctica. *Contributions to Mineralogy and Petrology*, 94, 427–437, <https://doi.org/10.1007/BF00376336>.
- Blum, T.B., Darling, J.R., Kelly, T.F., Larson, D.J., Moser, D.E., Perez-Huerta, A., Prosa, T.J., Reddy, S.M., Reinhard, D.A., and Saxey, D.W. (2018a) Best practices for reporting atom probe analysis of geological materials. *Microstructural Geochronology*, 232, 369–373.
- Blum, T., Reinhard, D.A., Chen, Y., Prosa, T.J., Larson, D.J., and Valley, J.W. (2018b) Uncertainty and sensitivity analysis for spatial and spectral processing of Pb isotopes in zircon by atom probe tomography. In D.E. Moser, F. Corfu, J.R. Darling, S.M. Reddy, and K. Tait, Eds., *Microstructural Geochronology: Planetary Records Down to Atom Scale*, p. 327–350. American Geophysical Union.
- Carson, C.J., Ague, J.J., and Coath, C.D. (2002) U-Pb geochronology from Tonagh Island, East Antarctica: Implications for the timing of ultra-high temperature metamorphism of the Napier Complex. *Precambrian Research*, 116, 237–263, [https://doi.org/10.1016/S0301-9268\(02\)00023-2](https://doi.org/10.1016/S0301-9268(02)00023-2).
- Clark, C., Taylor, R.J., Kylander-Clark, A.R., and Hacker, B.R. (2018) Prolonged ( $>100$  Ma) ultrahigh temperature metamorphism in the Napier Complex, East Antarctica: A petrochronological investigation of Earth's hottest crust. *Journal of Metamorphic Geology*, 36, 1117–1139, <https://doi.org/10.1111/jmg.12430>.
- Clark, C., Taylor, R.J., Johnson, T.E., Harley, S.L., Fitzsimons, I.C., and Oliver, L. (2019) Testing the fidelity of thermometers at ultrahigh temperatures. *Journal of Metamorphic Geology*, 37, 917–934, <https://doi.org/10.1111/jmg.12486>.
- Crameri, F. (2018) Scientific colour maps. Zenodo, v. 10.
- Dachille, F., Simons, P., and Roy, R. (1968) Pressure-temperature studies of anatase, brookite, rutile and  $\text{TiO}_2$ -II. *American Mineralogist*, 53, 1929–1939.
- Daneu, N., Rečnik, A., and Mader, W. (2014) Atomic structure and formation mechanism of (101) rutile twins from Diamantina (Brazil). *American Mineralogist*, 99, 612–624, <https://doi.org/10.2138/am.2014.4672>.
- Demartin, F., Pilati, T., Diella, V., Donzelli, S., and Gramaccioli, C.M. (1991) Alpine monazite: Further data. *Canadian Mineralogist*, 29, 61–67.
- Dubosq, R., Rogowitz, A., Schweinar, K., Gault, B., and Schneider, D.A. (2019) A 2D and 3D nanostructural study of naturally deformed pyrite: Assessing the links between trace element mobility and defect structures. *Contributions to Mineralogy and Petrology*, 174, 72, <https://doi.org/10.1007/s00410-019-1611-5>.
- Erickson, T., Pearce, M., Taylor, R., Timms, N.E., Clark, C., Reddy, S., and Buick, I. (2015) Deformed monazite yields high-temperature tectonic ages. *Geology*, 43, 383–386, <https://doi.org/10.1130/G36533.1>.
- Fougerouse, D., Reddy, S.M., Saxey, D.W., Erickson, T.M., Kirkland, C.L., Rickard, W.D.A., Seydoux-Guillaume, A.M., Clark, C., and Buick, I.S. (2018) Nanoscale distribution of Pb in monazite revealed by atom probe microscopy. *Chemical Geology*, 479, 251–258, <https://doi.org/10.1016/j.chemgeo.2018.01.020>.
- Fougerouse, D., Reddy, S., Seydoux-Guillaume, A.-M., Kirkland, C., Erickson, T., Saxey, D., Rickard, W., Jacob, D., Leroux, H., and Clark, C. (2021a) Mechanical twinning of monazite expels radiogenic lead. *Geology*, 49, 417–421, <https://doi.org/10.1130/G48400.1>.
- Fougerouse, D., Reddy, S.M., Aylmore, M., Yang, L., Guagliardo, P., Saxey, D.W., Rickard, W.D., and Timms, N. (2021b) A new kind of invisible gold in pyrite hosted in deformation-related dislocations. *Geology*, 49, 1225–1229, <https://doi.org/10.1130/G49028.1>.
- Fougerouse, D., Saxey, D.W., Rickard, W.D., Reddy, S.M., and Verberne, R.



- (2021c) Standardizing spatial reconstruction parameters for the atom probe analysis of common minerals. *Microscopy and Microanalysis*, 28, 1221–1230.
- Grand'Homme, A., Janots, E., Seydoux-Guillaume, A.-M., Guillaume, D., Bosse, V., and Magnin, V. (2016) Partial resetting of the U-Th-Pb systems in experimentally altered monazite: Nanoscale evidence of incomplete replacement. *Geology*, 44, 431–434, <https://doi.org/10.1130/G37770.1>.
- Harley, S.L. (2016) A matter of time: The importance of the duration of UHT metamorphism. *Journal of Mineralogical and Petrological Sciences*, 111, 50–72, <https://doi.org/10.2465/jmps.160128>.
- Harley, S.L. and Black, L.P. (1987) The Archaean geological evolution of Enderby Land, Antarctica. In R.G. Park and J. Tarney, Eds., *Evolution of the Lewisian and Comparable Precambrian high Grade Terrains*, 27th ed., 285–296. Geological Society of London.
- Harley, S.L. and Motoyoshi, Y. (2000) Al zoning in orthopyroxene in a sapphirine quartzite: Evidence for >1120 °C UHT metamorphism in the Napier Complex, Antarctica, and implications for the entropy of sapphirine. *Contributions to Mineralogy and Petrology*, 138, 293–307, <https://doi.org/10.1007/s004100050564>.
- Hart, E., Storey, C., Bruand, E., Schertl, H.P., and Alexander, B.D. (2016) Mineral inclusions in rutile: A novel recorder of HP-UHP metamorphism. *Earth and Planetary Science Letters*, 446, 137–148, <https://doi.org/10.1016/j.epsl.2016.04.035>.
- Hart, E., Storey, C., Harley, S.L., and Fowler, M. (2018) A window into the lower crust: Trace element systematics and the occurrence of inclusions/intergrowths in granulite-facies rutile. *Gondwana Research*, 59, 76–86, <https://doi.org/10.1016/j.gr.2018.02.021>.
- Hellman, O.C., Vandenbroucke, J.A., Rüsing, J., Isheim, D., and Seidman, D.N. (2000) Analysis of three-dimensional atom-probe data by the proximity histogram. *Microscopy and Microanalysis*, 6, 437–444, <https://doi.org/10.1007/S100050010051>.
- Hlava, P., Prinz, M., and Keil, K. (1972) Niobian rutile in an Apollo 14 KREEP fragment. *Meteoritics*, 7, 479–486, <https://doi.org/10.1111/j.1945-5100.1972.tb00128.x>.
- Hokada, T. (2001) Feldspar thermometry in ultrahigh-temperature metamorphic rocks: Evidence of crustal metamorphism attaining ~1100 °C in the Archaean Napier Complex, East Antarctica. *American Mineralogist*, 86, 932–938, <https://doi.org/10.2138/am-2001-0718>.
- Huang, T., Lee, J.-S., Kung, J., and Lin, C.-M. (2010) Study of monazite under high pressure. *Solid State Communications*, 150, 1845–1850, <https://doi.org/10.1016/j.ssc.2010.06.042>.
- Ikeda, J.A.S. and Chiang, Y.M. (1993) Space charge segregation at grain boundaries in titanium dioxide: I. relationship between lattice defect chemistry and space charge potential. *Journal of the American Ceramic Society*, 76, 2437–2446, <https://doi.org/10.1111/j.1151-2916.1993.tb03964.x>.
- Ikeda, J.A.S., Chiang, Y.M., Garratt-Reed, A.J., and Sande, J.B.V. (1993) Space charge segregation at grain boundaries in titanium dioxide: II, model experiments. *Journal of the American Ceramic Society*, 76, 2447–2459, <https://doi.org/10.1111/j.1151-2916.1993.tb03965.x>.
- James, P. and Black, L., Eds. (1981) *Archaean Geology: Second International Symposium*, Perth 1980, 515 p. Geological Society of Australia.
- Janots, E., Engi, M., Berger, A., Allaz, J., Schwarz, J.O., and Spandler, C. (2008) Prograde metamorphic sequence of REE minerals in pelitic rocks of the Central Alps: Implications for allanite–monazite–xenotime phase relations from 250 to 610 °C. *Journal of Metamorphic Geology*, 26, 509–526, <https://doi.org/10.1111/j.1525-1314.2008.00774.x>.
- Janots, E., Berger, A., Gnos, E., Whitehouse, M., Lewin, E., and Pettker, T. (2012) Constraints on fluid evolution during metamorphism from U-Th-Pb systematics in Alpine hydrothermal monazite. *Chemical Geology*, 326–327, 61–71, <https://doi.org/10.1016/j.chemgeo.2012.07.014>.
- Kliwer, K. (1965) Space charge in ionic crystals. II. The electron affinity and impurity accumulation. *Physical Review*, 140, A1241–A1246, <https://doi.org/10.1103/PhysRev.140.A1241>.
- Kooijman, E., Mezger, K., and Berndt, J. (2010) Constraints on the U-Pb systematics of metamorphic rutile from in situ LA-ICP-MS analysis. *Earth and Planetary Science Letters*, 293, 321–330, <https://doi.org/10.1016/j.epsl.2010.02.047>.
- Kusiak, M.A., Dunkley, D.J., Wirth, R., Whitehouse, M.J., Wilde, S.A., and Marquardt, K. (2015) Metallic lead nanospheres discovered in ancient zircons. *Proceedings of the National Academy of Sciences*, 112(16), 4958–4963.
- Kusiak, M., Kovaleva, E., Wirth, R., Klötzli, U., Dunkley, D., Yi, K., and Lee, S. (2019) Lead oxide nanospheres in seismically deformed zircon grains. *Geochimica et Cosmochimica Acta*, 262, 20–30, <https://doi.org/10.1016/j.gca.2019.07.026>.
- Kusiak, M.A., Wirth, R., Wilde, S.A., and Pidgeon, R.T. (2023) Metallic lead (Pb) nanospheres discovered in Hadean and Eoarchean zircon crystals at Jack Hills. *Scientific Reports*, 13(1), 895.
- Larere, A., Guillope, M., and Masuda-Jindo, K. (1988) Segregation energies of phosphorus and sulfur in various relaxed structures of grain boundaries in Ni by tight-binding approximation. *Le Journal de Physique Colloques*, 49, C5-447–C5-450.
- Lloyd, G.E., Farmer, A.B., and Mainprice, D. (1997) Misorientation analysis and the formation and orientation of subgrain and grain boundaries. *Tectonophysics*, 279, 55–78, [https://doi.org/10.1016/S0040-1951\(97\)00115-7](https://doi.org/10.1016/S0040-1951(97)00115-7).
- Lyon, I.C., Kusiak, M.A., Wirth, R., Whitehouse, M.J., Dunkley, D.J., Wilde, S.A., Schaumlöffel, D., Malherbe, J., and Moore, K.L. (2019) Pb nanospheres in ancient zircon yield model ages for zircon formation and Pb mobilization. *Scientific Reports*, 9, 13702, <https://doi.org/10.1038/s41598-019-49882-8>.
- Mannucci, G., Diella, V., Gramaccioli, C.M., and Pilati, T. (1986) A comparative study of some pegmatitic and fissure monazite from the Alps. *Canadian Mineralogist*, 24, 469–474.
- Meinhold, G. (2010) Rutile and its applications in Earth sciences. *Earth-Science Reviews*, 102, 1–28, <https://doi.org/10.1016/j.earscirev.2010.06.001>.
- Mitchell, R.J. and Harley, S.L. (2017) Zr-in-rutile resetting in aluminosilicate bearing ultra-high temperature granulites: Refining the record of cooling and hydration in the Napier Complex, Antarctica. *Lithos*, 272–273, 128–146, <https://doi.org/10.1016/j.lithos.2016.11.027>.
- Mosenfelder, J.L., Schertl, H.-P., Smyth, J.R., and Liou, J.G. (2005) Factors in the preservation of coesite: The importance of fluid infiltration. *American Mineralogist*, 90, 779–789, <https://doi.org/10.2138/am.2005.1687>.
- Ni, Y., Hughes, J.M., and Mariano, A.N. (1995) Crystal chemistry of the monazite and xenotime structures. *American Mineralogist*, 80, 21–26, <https://doi.org/10.2138/am-1995-1-203>.
- Pape, J., Mezger, K., and Robyr, M. (2016) A systematic evaluation of the Zr-in-rutile thermometer in ultra-high temperature (UHT) rocks. *Contributions to Mineralogy and Petrology*, 171, 44, <https://doi.org/10.1007/s00410-016-1254-8>.
- Peterman, E.M., Reddy, S.M., Saxey, D.W., Snoeyenbos, D.R., Rickard, W.D., Fougereuse, D., and Kylander-Clark, A.R. (2016) Nanogeochronology of discordant zircon measured by atom probe microscopy of Pb-enriched dislocation loops. *Science Advances*, 2, e1601318, <https://doi.org/10.1126/sciadv.1601318>.
- Poitras, F., Chenery, S., and Bland, D.J. (1996) Contrasted monazite hydrothermal alteration mechanisms and their geochemical implications. *Earth and Planetary Science Letters*, 145, 79–96, [https://doi.org/10.1016/S0012-821X\(96\)00193-8](https://doi.org/10.1016/S0012-821X(96)00193-8).
- Prior, D.J., Wheeler, J., Peruzzo, L., Spiess, R., and Storey, C. (2002) Some garnet microstructures: An illustration of the potential of orientation maps and misorientation analysis in microstructural studies. *Journal of Structural Geology*, 24, 999–1011, [https://doi.org/10.1016/S0191-8141\(01\)00087-6](https://doi.org/10.1016/S0191-8141(01)00087-6).
- Reddy, S.M., Timms, N.E., Pantleon, W., and Trimby, P. (2007) Quantitative characterization of plastic deformation of zircon and geological implications. *Contributions to Mineralogy and Petrology*, 153, 625–645, <https://doi.org/10.1007/s00410-006-0174-4>.
- Reddy, S.M., Saxey, D.W., Rickard, W.D., Fougereuse, D., Montalvo, S.D., Verberne, R., and Van Riessen, A. (2020) Atom probe tomography: Development and application to the geosciences. *Geostandards and Geoanalytical Research*, 44, 5–50, <https://doi.org/10.1111/ggr.12313>.
- Rickard, W.D.A., Reddy, S.M., Saxey, D.W., Fougereuse, D., Timms, N.E., Daly, L., Peterman, E., Cavosie, A.J., and Jourdan, F. (2020) Novel applications of FIB-SEM-Based ToF-SIMS in atom probe tomography workflows. *Microscopy and Microanalysis*, 26, 750–757, <https://doi.org/10.1017/S1431927620000136>.
- Seydoux-Guillaume, A.-M., Paquette, J.-L., Wiedenbeck, M., Montel, J.-M., and Heinrich, W. (2002a) Experimental resetting of the U-Th-Pb systems in monazite. *Chemical Geology*, 191, 165–181, [https://doi.org/10.1016/S0009-2541\(02\)00155-9](https://doi.org/10.1016/S0009-2541(02)00155-9).
- Seydoux-Guillaume, A.M., Wirth, R., Nasdala, L., Gottschalk, M., Montel, J.M., and Heinrich, W. (2002b) An XRD, TEM and Raman study of experimentally annealed natural monazite. *Physics and Chemistry of Minerals*, 29, 240–253, <https://doi.org/10.1007/s00269-001-0232-4>.
- Seydoux-Guillaume, A.M., Wirth, R., Heinrich, W., and Montel, J.M. (2002c) Experimental determination of thorium partitioning between monazite and xenotime using analytical electron microscopy and X-ray diffraction Rietveld analysis. *European Journal of Mineralogy*, 14, 869–878, <https://doi.org/10.1127/0935-1221/2002/0014-0869>.
- Seydoux-Guillaume, A.M., Goncalves, P., Wirth, R., and Deutsch, A. (2003) Transmission electron microscope study of polyphase and discordant monazites: Site-specific specimen preparation using the focused ion beam technique. *Geology*, 31, 973–976, <https://doi.org/10.1130/G19582.1>.
- Seydoux-Guillaume, A.M., Wirth, R., Deutsch, A., and Schärer, U. (2004) Microstructure of 24–1928 Ma concordant monazites: Implications for geochronology and nuclear waste deposits. *Geochimica et Cosmochimica Acta*, 68, 2517–2527, <https://doi.org/10.1016/j.gca.2003.10.042>.
- Seydoux-Guillaume, A.-M., Montel, J.-M., Bingen, B., Bosse, V., De Parseval, P., Paquette, J.-L., Janots, E., and Wirth, R. (2012) Low-temperature alteration of monazite: Fluid mediated coupled dissolution-precipitation, irradiation damage, and disturbance of the U-Pb and Th-Pb chronometers. *Chemical Geology*, 330–331, 140–158, <https://doi.org/10.1016/j.chemgeo.2012.07.031>.
- Seydoux-Guillaume, A.-M., Deschanel, X., Baumier, C., Neumeier, S., Weber, W.J., and Peugeot, S. (2018) Why natural monazite never becomes amorphous: Experimental evidence for alpha self-healing. *American Mineralogist*, 103, 824–827, <https://doi.org/10.2138/am-2018-6447>.

- Seydoux-Guillaume, A.-M., Fougereuse, D., Laurent, A., Gardés, E., Reddy, S., and Saxey, D. (2019) Nanoscale resetting of the Th/Pb system in an isotopically-closed monazite grain: A combined atom probe and transmission electron microscopy study. *Geoscience Frontiers*, 10, 65–76, <https://doi.org/10.1016/j.gsf.2018.09.004>.
- Sheraton, J.W., Thomson, J.W., and Collerson, K.D. (1987) Mafic dyke swarms of Antarctica. In H.C. Halls and W.F. Fahrig, Eds., *Mafic dyke swarms. A collection of papers based on the proceedings of an international conference held at Erindale College, University of Toronto, Ontario, Canada, June 1985*, p. 419–432. Geological Association of Canada.
- Smye, A.J. and Stockli, D.F. (2014) Rutile U-Pb age depth profiling: A continuous record of lithospheric thermal evolution. *Earth and Planetary Science Letters*, 408, 171–182, <https://doi.org/10.1016/j.epsl.2014.10.013>.
- Sutton, A.P. and Balluffi, R.W. (1995) *Interfaces in Crystalline Materials*, 819 p. Clarendon Press.
- Suzuki, S., Abiko, K., and Kimura, H. (1981) Phosphorus segregation related to the grain boundary structure in an Fe-P alloy. *Scripta Metallurgica*, 15, 1139–1143, [https://doi.org/10.1016/0036-9748\(81\)90175-7](https://doi.org/10.1016/0036-9748(81)90175-7).
- Suzuki, K., Ichihara, M., and Takeuchi, S. (1991) High-resolution electron microscopy of lattice defects in TiO<sub>2</sub> and SnO<sub>2</sub>. *Philosophical Magazine A*, 63, 657–665, <https://doi.org/10.1080/01418619108213906>.
- Swope, R.J., Smyth, J.R., and Larson, A.C. (1995) H in rutile-type compounds: I. Single-crystal neutron and X-ray diffraction study of H in rutile. *American Mineralogist*, 80, 448–453, <https://doi.org/10.2138/am-1995-5-604>.
- Tacchetto, T., Reddy, S.M., Saxey, D.W., Fougereuse, D., Rickard, W.D.A., and Clark, C. (2021) Disorientation control on trace element segregation in fluid-affected low-angle boundaries in olivine. *Contributions to Mineralogy and Petrology*, 176, 59, <https://doi.org/10.1007/s00410-021-01815-3>.
- Taylor, R.J., Reddy, S.M., Saxey, D.W., Rickard, W.D., Tang, F., Borlina, C.S., Fu, R.R., Weiss, B.P., Bagot, P., and Williams, H.M. (2023) Direct age constraints on the magnetism of Jack Hills zircon. *Science Advances*, 9, eadd1511.
- Thompson, K., Lawrence, D., Larson, D.J., Olson, J.D., Kelly, T.F., and Gorman, B. (2007) In situ site-specific specimen preparation for atom probe tomography. *Ultramicroscopy*, 107, 131–139, <https://doi.org/10.1016/j.ultramicro.2006.06.008>.
- Triebold, S., von Eynatten, H., Luvizotto, G.L., and Zack, T. (2007) Deducing source rock lithology from detrital rutile geochemistry: An example from the Erzgebirge, Germany. *Chemical Geology*, 244, 421–436, <https://doi.org/10.1016/j.chemgeo.2007.06.033>.
- Turuani, M.J., Laurent, A.T., Seydoux-Guillaume, A.M., Fougereuse, D., Saxey, D., Reddy, S.M., Harley, S.L., Reynaud, S., and Rickard, W.D.A. (2022) Partial retention of radiogenic Pb in galena nanocrystals explains discordance in monazite from Napier Complex (Antarctica). *Earth and Planetary Science Letters*, 588, 117567, <https://doi.org/10.1016/j.epsl.2022.117567>.
- Turuani, M.J., Seydoux-Guillaume, A.-M., Laurent, A.T., Reddy, S., Harley, S., Fougereuse, D., Saxey, D., Gouy, S., Parseval, D., and Reynaud, S. (2023) Nanoscale features revealed by a multiscale characterization of discordant monazite highlight mobility mechanisms of Th and Pb. *Contributions to Mineralogy and Petrology*, 178, 31.
- Valley, J.W., Cavoie, A.J., Ushikubo, T., Reinhard, D.A., Lawrence, D.F., Larson, D.J., Clifton, P.H., Kelly, T.F., Wilde, S.A., Moser, D.E., and others. (2014) Hadean age for a post-magma-ocean zircon confirmed by atom-probe tomography. *Nature Geoscience*, 7, 219–223, <https://doi.org/10.1038/ngeo2075>.
- Verberne, R., Saxey, D.W., Reddy, S.M., Rickard, W.D.A., Fougereuse, D., and Clark, C. (2019) Analysis of natural rutile (TiO<sub>2</sub>) by laser-assisted atom probe tomography. *Microscopy and Microanalysis*, 25, 539–546, <https://doi.org/10.1017/S1431927618015477>.
- Verberne, R., Reddy, S., Saxey, D., Fougereuse, D., Rickard, W., Plavska, D., Agangi, A., and Kylander-Clark, A. (2020) The geochemical and geochronological implications of nanoscale trace-element clusters in rutile. *Geology*, 48, 1126–1130, <https://doi.org/10.1130/G48017.1>.
- Verberne, R., Reddy, S.M., Saxey, D.W., Fougereuse, D., Rickard, W.D., Quadir, Z., Evans, N.J., and Clark, C. (2022) Dislocations in minerals: Fast-diffusion pathways or trace-element traps? *Earth and Planetary Science Letters*, 584, 117517, <https://doi.org/10.1016/j.epsl.2022.117517>.
- Verberne, R., van Schrojenstein Lantman, H.W., Reddy, S.M., Alvaro, M., Wallis, D., Fougereuse, D., Langone, A., Saxey, D.W., and Rickard, W.D. (2023) Trace-element heterogeneity in rutile linked to dislocation structures: Implications for Zr-in-rutile geothermometry. *Journal of Metamorphic Geology*, 41, 3–24, <https://doi.org/10.1111/jmg.12686>.
- Watson, E.B., Wark, D.A., and Thomas, J.B. (2006) Crystallization thermometers for zircon and rutile. *Contributions to Mineralogy and Petrology*, 151, 413–433, <https://doi.org/10.1007/s00410-006-0068-5>.
- Zack, T., Moraes, R., and Kronz, A. (2004a) Temperature dependence of Zr in rutile: Empirical calibration of a rutile thermometer. *Contributions to Mineralogy and Petrology*, 148, 471–488, <https://doi.org/10.1007/s00410-004-0617-8>.
- Zack, T., von Eynatten, H., and Kronz, A. (2004b) Rutile geochemistry and its potential use in quantitative provenance studies. *Sedimentary Geology*, 171, 37–58, <https://doi.org/10.1016/j.sedgeo.2004.05.009>.
- Zaffiro, G., Angel, R.J., and Alvaro, M. (2019) Constraints on the equations of state of stiff anisotropic minerals: Rutile, and the implications for rutile elastic barometry. *Mineralogical Magazine*, 83, 339–347, <https://doi.org/10.1180/mgm.2019.24>.

MANUSCRIPT RECEIVED JUNE 1, 2023

MANUSCRIPT ACCEPTED DECEMBER 14, 2023

ACCEPTED MANUSCRIPT ONLINE DECEMBER 19, 2023

MANUSCRIPT HANDLED BY CLAIRE E. BUCHOLZ

## Endnote:

<sup>1</sup>Deposit item AM-24-99085. Online Materials are free to all readers. Go online, via the table of contents or article view, and find the tab or link for supplemental materials.